Role of electron-phonon coupling in finite-temperature dielectric functions of Au, Ag, and Cu

Meng Xu,[1] Jia-Yue Yang,[2] Shangyu Zhang,[1] and Linhua Liu[1,3,*]

[1]*School of Energy Science and Engineering, Harbin Institute of Technology, Harbin 150001, China*

[2]*Institute of Mineral Engineering, Rheinisch-Westfaelische Technische Hochschule (RWTH) Aachen University, Aachen 52064, Germany*

[3]*Department of Physics, Harbin Institute of Technology, Harbin 150001, China*

(Received 12 May 2017; published 26 September 2017)

Realistic representation of finite temperature dielectric functions of noble metals is crucial in describing the optical properties of advancing applications in plasmonics and optical metamaterials. However, the atomistic origins of the temperature dependence of noble metals' dielectric functions still lack full explanation. In this paper, we implement electronic structure calculations as well as ellipsometry experiments to study the finite temperature dielectric functions of noble metals Au, Ag, and Cu. Theoretically, the intraband dielectric function is described by the Drude model, of which the important quantity electron lifetime is obtained by considering the electron-phonon, electron-electron, and electron-surface scattering mechanism. The electron-phonon coupling is key to determining the temperature dependence of electron lifetime and intraband dielectric function. For the interband dielectric function, it arises from the electronic interband transition. Due to the limitation of incorporating electron-phonon coupling into the interband transition scheme, the temperature dependence of the interband dielectric function is mainly determined by the thermal expansion effect. Experimentally, variable angle spectroscopic ellipsometry measures the dielectric functions of Au and Ag over the temperature range of 300–700 K and spectral range of 2–20 μm. Those experimental measurements are consistent with theoretical results and thus verify the theoretical models for the finite temperature dielectric function.

DOI: 10.1103/PhysRevB.96.115154

I. INTRODUCTION

The noble metals Au, Ag, and Cu are widely used in applications ranging from optoelectronics, catalysis, plasmonics to optical metamaterials [1–3]. The dielectric functions of the noble metals play an important role in those applications since they are basic input parameters for the optical simulation and design process. Since most of those applications operate at high temperature conditions, the dielectric functions at high temperatures are thus required, but nowadays, most theoretical models are based on the optical properties of noble metals at room temperature, which can lead to large errors in estimating of the efficiency and performance. Recently, it has been reported that the variation of optical constants of noble metals can lead to a large difference in the optical properties of plasmonic nanoparticles [4]. Therefore, the accurate prediction of optical properties at elevated temperatures can not only foster the deep understanding of the underlying physical process, but also improve the accurate modeling of structures for high temperature applications.

In the infrared spectral range, the optical absorption of noble metals mainly arises from the response of free electrons to the incident electromagnetic wave, which can be described by the Drude model. The scattering mechanism for free electrons includes collisions with phonons, other electrons, lattice defects, and impurities [5]. The typical method to obtain the electron scattering rate is to fit experimental results of noble metals to the Drude model, which is widely used to obtain the electron scattering rate of Au [6,7] and Ag [8,9]. Due to experimental uncertainties, such as surface morphology, thermal oxidation, and self-radiation, the obtained electron scattering rates differ from each other. Based on classical electron gas theory, electron-phonon scattering has been investigated by Holstein [10], and the electron-electron scattering has been studied by Lawrence [11]. More advanced calculations of electron-phonon and electron-electron scattering employ state-of-the-art first principles. The electron-electron scattering rate can be calculated by the single-particle Green function and the screened Coulomb interaction GW approximation [12,13], while the calculation of electron-phonon scattering rate from first principles is computationally expensive, since the latter requires fine sampling over the Brillouin zone. Recently, the computation has been reduced by the maximally localized Wannier functions as implemented in the electron-phonon Wannier (EPW) package [14]. Such electron-phonon coupling calculation has been used in the recent first-principles calculation of thermal conductivity [15,16] and electrical conductivity [17] of noble metals.

To predict the temperature-dependent dielectric functions of noble metals at high temperatures, the key is to understand the electron-phonon interaction. In this paper, we use electronic structure calculations to study the electron-phonon interaction (EPI) and its influence on electronic energy state and relaxation time, and the electron-electron scattering rates are calculated by the GW approximation. The intraband dielectric functions of noble metals are calculated by substituting the electron lifetime into the Drude model. The interband dielectric function arising from the electron's band-to-band transition can be calculated following Fermi's golden rule. By superimposing the intraband and interband dielectric function, the dielectric functions of noble metals are determined. To verify the theoretical results, the spectroscopic ellipsometry experiments on dielectric functions of Au and Ag are performed.

II. COMPUTATIONAL METHODOLOGY

In noble metals, the extended s and p electronic states are hybridized with the more localized d electronic states

*lhliu@hit.edu.cn

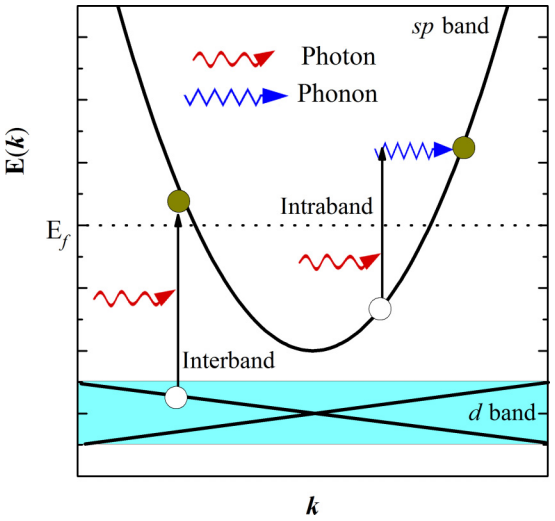

FIG. 1. Schematics of the interband and intraband transition in noble metals.

to form a composite band [18]. The interband transitions from occupied states in the d band to unoccupied states in the sp band give rise to an absorption peak in the visible-ultraviolet spectral range, while the infrared absorption mainly arises from the intraband transition within the sp band [19]. As shown in Fig. 1, in order to satisfy the energy and momentum conservation, an additional phonon scattering process is needed during the intraband transition; thus, the electron-phonon scattering should be taken into account during the calculation of intraband absorption. The dielectric function of noble metals can be expressed as [20]

$$\varepsilon(\omega) = \varepsilon^f(\omega) + \varepsilon^b(\omega), \tag{1}$$

where $\varepsilon^f(\omega)$ represents the intraband or free electron term and arises from optical transitions between electron states in one partially filled band, and $\varepsilon^b(\omega)$ is the interband contribution and is contributed by the band-to-band transition of a "bound electron".

A. Intraband transition

The Drude-Sommerfeld model regards metal as a classical gas of electrons, with the assumption of spherical Fermi surface [21]. Despite the intervention of the d bands to the sp bands of noble metals, the Fermi surface of noble metals is roughly equivalent to the free-electron Fermi sphere. Therefore, the free electron intraband dielectric function of noble metals can be well described by the Drude model as [21]

$$\varepsilon = 1 - \frac{\Omega_p^2}{(\omega^2 + i\Gamma_D\omega)}, \tag{2}$$

where Ω_p is the plasma frequency for intraband transitions, $\Gamma_D = 1/\tau_D$ is the electron scattering rate, and τ_D is the electron relaxation time. The imaginary part of the dielectric function can be expressed as

$$\varepsilon_2 = \frac{1}{\omega\tau_D}\frac{\Omega_p^2}{\omega^2 + \tau_D^{-2}}. \tag{3}$$

In order to theoretically predict the dielectric function without empirical parameters, the underlying physical mechanisms of Ω_p and τ_D should be investigated and their values should be calculated by first principles. Based on the linear response theory, the plasma frequency Ω_p can be expressed as [22]

$$\Omega^2_{p,\alpha\beta} = -\frac{4\pi e^2}{V\hbar^2}\sum_{n\mathbf{k}} 2g_{\mathbf{k}}\frac{\partial f(E_{n\mathbf{k}})}{\partial E}\left(\mathbf{e}_\alpha\frac{\partial E_{n\mathbf{k}}}{\partial \mathbf{k}}\right)\left(\mathbf{e}_\beta\frac{\partial E_{n\mathbf{k}}}{\partial \mathbf{k}}\right), \tag{4}$$

where $E_{n\mathbf{k}}$ is the eigenenergy of state with band index n and wave vector $\mathbf{k}$, $f(E_{n\mathbf{k}})$ is the Fermi-Dirac distribution, $\mathbf{e}_\alpha$ and $\mathbf{e}_\beta$ are Cartesian directions, and V is the volume of unit cell. The factor of 2 accounts for the spin degeneracy, and the weighting factor $g_{\mathbf{k}}$ accounts for the summation performed over the irreducible part of the Brillouin zone.

The calculations of intraband plasma frequency Ω_p were performed in the Vienna *Ab initio* Simulation Package (VASP) [23]. The projector augmented-wave (PAW) method is used, and the Cu, Ag, and Au atoms were described by the Perdew-Burke-Ernzerhof (PBE) exchange and correlation potential within the framework of the generalized gradient approximation (GGA) [24]. The energy cutoff was set to be 500 eV, and a 48 × 48 × 48 Monkhorst-Pack grid was generated automatically over the entire first Brillouin zone to ensure the convergence. The convergence test can be found in the Supplemental Material [25].

The scattering mechanism for free electrons includes collisions with phonons, other electrons, or lattice defects and impurities. In addition, due to the strong absorption of metals in the infrared spectral range, the surface scattering plays an important role, so that the total scattering rate can be expressed as

$$\frac{1}{\tau_D} = \frac{1}{\tau_s} + \frac{1}{\tau_{\text{bulk}}}, \tag{5}$$

where $1/\tau_s$ is the surface scattering rate, and $1/\tau_{\text{bulk}}$ is the bulk scattering rate. According to a previous study [5], the bulk scattering rate is contributed by three independent components

$$\frac{1}{\tau_{\text{bulk}}} = \frac{1}{\tau_{\text{ep}}} + \frac{1}{\tau_{\text{ee}}} + \frac{1}{\tau_i}, \tag{6}$$

where τ_{ep}^{-1} is the scattering rate arising from electron-phonon interaction, which is temperature dependent but frequency independent, τ_{ee}^{-1} is due to electron-electron scattering, which is temperature independent but frequency dependent, and τ_i^{-1} is due to electron-defect scattering. Due to the relatively strong electron-phonon scattering, τ_i^{-1} is negligible at elevated temperature. The calculations of electron-phonon and electron-electron scattering rate are discussed in the following parts.

1. Electron-phonon scattering

The temperature dependence of the dielectric function can be understood by the interpretation of electron-phonon scattering. As temperature increases, the lattice vibration is enhanced, and electron-phonon scattering is increased. According to the electron-phonon gas theory of Holstein [10],

this scattering rate is expressed as [26]

$$\frac{1}{\tau_{\rm ep}} = \frac{1}{\tau_0}\left[\frac{2}{5} + 4\left(\frac{T}{\Theta}\right)^5 \int_0^{\Theta/T} \frac{z^4 dz}{e^z - 1}\right], \tag{7}$$

where Θ is the Debye temperature, and $1/\tau_0$ is a material dependent constant. The integral variable z is defined as $z = \hbar\omega_{\mathbf{q}}/k_B T$ [26], with an upper limit of Θ/T. Here, $\omega_{\mathbf{q}}$ is the phonon frequency of wave vector $\boldsymbol{q}$, $\hbar$ is the reduced Planck constant, and k_B is the Boltzmann constant. Since the determination of $1/\tau_0$ needs experimental data, Eq. (7) cannot be used in the prediction of the electron-phonon scattering rate. The state-of-the-art accurate calculations of the electron scattering rate of solids rely on the computation of electron self-energy by electron-phonon coupling. The electron self-energy (Σ) at temperature T is given by [14]

$$\begin{aligned}\Sigma_{n\mathbf{k}}(T) = \frac{2\pi}{\hbar}\sum_{n\mathbf{k}'}\sum_{\mathbf{q}v} w_{\mathbf{q}}\left|g^{SE}_{mn,v}(\mathbf{k}\mathbf{k}',\mathbf{q})\right|^2 \\ \times\left[\frac{n_{\mathbf{q}v}(T) + f_{m\mathbf{k}'}(T)}{\varepsilon_{n\mathbf{k}} - \varepsilon_{m\mathbf{k}'} + \omega_{\mathbf{q}v} - i\eta}\right. \\ \left. + \frac{n_{\mathbf{q}v}(T) + 1 - f_{m\mathbf{k}'}(T)}{\varepsilon_{n\mathbf{k}} - \varepsilon_{m\mathbf{k}'} - \omega_{\mathbf{q}v} - i\eta}\right],\end{aligned} \tag{8}$$

where $\varepsilon_{n\mathbf{k}}$ and $\varepsilon_{m\mathbf{k}'}$ are the eigenvalues of Kohn-Sham (KS) states $n\mathbf{k}$ and $m\mathbf{k}$', respectively, $\omega_{\mathbf{q}v}$ is the phonon frequency of branch v and wave vector $\mathbf{q}$, $n_{\mathbf{q}v}$ is the Bose-Einstein distribution, $f_{m\mathbf{k}+\mathbf{q}}$ is the Fermi-Dirac distribution, $w_{\mathbf{k}}$ are the weights of $\mathbf{k}$-points, and $g^{SE}_{mn,v}(\mathbf{k},\mathbf{q})$ is the electron-phonon matrix element.

With the calculated electron self-energy $\Sigma_{n\mathbf{k}}(T)$, one can obtain the electron scattering rate by $\tau^{-1}_{\rm ep}(n\mathbf{k},T) = 2{\rm Im}\Sigma_{n\mathbf{k}}(T)$. Here, $\tau^{-1}_{\rm ep}(n\mathbf{k},T)$ represents the electron scattering rate of band n and wave vector $\mathbf{k}$ at temperature T. Thereafter, the frequency independent electron-phonon scattering rate $\tau^{-1}_{\rm ep}$ is given by an energy average in the vicinity of Fermi surface [27]

$$\tau^{-1}_{\rm ep}(T) = \int_{-\infty}^{+\infty} \tau^{-1}_{\rm ep}(\varepsilon,T)\left(-\frac{\partial f}{\partial \varepsilon}\right)d\varepsilon, \tag{9}$$

where $f(\varepsilon)$ is the Fermi-Dirac function.

The EPI calculations were accomplished by Quantum Espresso [28] and EPW [14] packages. The wave functions were expanded into plane waves, and core electrons were simulated by norm-conserving pseudopotentials [29]. Owing to the advantage of maximally localized Wannier functions (MLWFs) [30], fine grids of $32 \times 32 \times 32$ $\mathbf{k}$-points and $20 \times 20 \times 20$ $\mathbf{q}$-points were used in the calculation of electron-phonon matrix elements. The kinetic energy cutoffs of 180 Ry for Cu and 90 Ry for Au and Ag were applied. The $3d$ electrons of Cu, $4d$ electrons of Ag, and $5d$ electrons of Au were included in the valence to make an accurate calculation of the electron-electron and electron-phonon scattering.

2. Electron-electron scattering

The electron-phonon scattering rate $\tau^{-1}_{\rm ep}$ dominates the electron scattering process in the midinfrared, and it is frequency independent. However, in the near infrared up to the interband absorption edge, τ^{-1}_{D} becomes strongly frequency dependent due to the contribution of electron-electron scattering. Based on the Born approximation and Thomas-Fermi screening of the Coulomb interaction, the scattering rate $\tau^{-1}_{\rm ee}$ is given by Lawrence [11] as

$$\frac{1}{\tau_{\rm ee}} = \frac{1}{12}\pi^3\Gamma\Delta\frac{1}{\hbar E_F}\left[(k_B T)^2 + \left(\frac{\hbar\omega}{2\pi}\right)^2\right], \tag{10}$$

where Γ, $\triangle$, and E_F are the average scattering probability, fractional umklapp scattering, and Fermi energy, respectively. The temperature-dependent term in $\tau^{-1}_{\rm ee}$ is small compared with the frequency-dependent term and is often neglected.

The free electron gas approximations are used during the derivation of Eq. (10), and the scattering rate from Eq. (10) deviates from experimental results to some extent. Nowadays, first-principles calculations based on GW approximation are widely used in the determination of electron self-energy arising from electron-electron scattering. For details about the GW approximation, one can refer to Refs. [12,13]. Once the GW calculation is accomplished, the electron scattering rate can be extracted from the imaginary part of electron self-energy ${\rm Im}\Sigma(\varepsilon_j)$ by [13]

$$\tau^{-1}_{\rm ee}(j) = 2|\langle j|{\rm Im}\Sigma(E_j)|j\rangle| = 2Z_j|\langle j|{\rm Im}\Sigma(\varepsilon_j)|j\rangle|, \tag{11}$$

where j is the KS eigenstate, and Z_j is the quasiparticle renormalization factor defined as

$$Z_j^{-1} = 1 - \langle j|\frac{\partial\Sigma(\omega)}{\partial\omega}\Big|_{\omega=\varepsilon_j}|j\rangle. \tag{12}$$

The GW calculations were performed in the YAMBO package with the ground state wave functions generated by the QE package. The single-shot GW (usually called G_0W_0) and real axis integration are used in this paper. Ground-state calculations are performed with a Monkhorst-Pack grid $16 \times 16 \times 16$ for the Brillouin zone and kinetic energy cutoffs of 180 Ry for Cu and 90 Ry for Au and Ag, and we included 40 empty bands in the calculations.

3. Surface scattering

In the infrared, where the electron mean free path $l = v_F\tau$ (v_F is the electron Fermi velocity) becomes comparable to or larger than the skin depth of the incident electromagnetic wave, the electron samples a nonlocal electric field [31]. This phenomenon is known as the anomalous skin effect [31,32]. Bennett *et al.* [33] investigated the infrared reflectance of silver films by anomalous skin effect theory. Ashcroft and Sturm [34] and Gamez and Ocana [35] have included such effect in the prediction of dielectric function of aluminum.

According to these studies, by assuming electrons scatter diffusely at the surface, the effect of surface scattering can be given as

$$\frac{1}{\tau_s} = \frac{3}{8}\left(\frac{v_F}{c}\right)\left(\frac{4\pi ne^2}{m_{\rm eff}}\right)^{1/2}, \tag{13}$$

where $m_{\rm eff}$ is the electron effective mass, and n is the density of a conduction electron. In this paper, $m_{\rm eff}$ is calculated by the relation $\Omega_p^2 = 4\pi ne^2/m_{\rm eff}$, and n is the number of conduction electrons in a unit cell divided by the volume of the unit cell. The number of conduction electrons is 1 for noble metals Cu,

Ag, and Au. The calculated effective mass m_{eff} for Au, Ag, and Cu are 1.07, 1.01, and 1.46, respectively, which are in good agreement with theoretical calculations of 1.10, 0.99, and 1.45 in Ref. [36].

B. Interband transition

In the visible-ultraviolet spectral range, the absorption of incident photons in metal arises from the electron's band-to-band transition. Based on Fermi's golden rule, the imaginary part ε_2 of the dielectric function can be described by [21]

$$\varepsilon_2(\omega) = (8\pi^2 e^2/m^2\omega^2 V)\sum_{c,v}|P_{c,v}|^2\delta(E_c - E_v - \hbar\omega), \quad (14)$$

where the subscripts c and v denote conduction band and valence band, P is the momentum transition matrix, $\hbar$ is the Planck's constant, V is the volume of the unit cell, m and e are the effective mass and charge of an electron, respectively. Winsemius *et al.* [37] and Christensen *et al.* [38] claimed that lattice expansion is the main source of temperature dependence of interband absorption of the noble metals. As the expansion of the lattice, the free-electron like bands will move towards lower energy, and d bands become narrower [38]. So in order to calculate the interband dielectric function at high temperature, the coefficients of thermal expansion of noble metals at corresponding temperature from experiments [39,40] are used. The calculation of interband transition was performed with VASP, and the setups were the same as those used previously in the calculation of intraband plasma frequency. Due to the heavy computing work, the independent-particle random phase approximation (RPA) was applied to compute the optical spectra, and an experimental scissor operator (SO) is applied to modify the optical spectra. The application of experimental thermal expansion and the SO makes the calculation not fully *ab initio*, but it makes the investigation of temperature effects of interband transition computational feasible. In fact, this paper is a combination of first principles and semiempirical assumptions.

III. ELLIPSOMETRY EXPERIMENT

To validate the above theoretical calculations, the dielectric functions of Au and Ag films were measured by variable angle spectroscopic ellipsometry (VASE). Au and Ag films with thicknesses of 150 nm were evaporated onto clean SiO_2 substrate at a pressure of 5.6×10^{-4} Pa. The film was deposited at a rate of 1.0 nm/s. The surface roughness and grain size of the samples are characterized by atomic force microscopy (AFM). The results of AFM are given in the Supplemental Material [25]. The derived root mean square (rms) surface roughness of the Au and Ag samples was 1.2 and 1.5 nm, respectively, and the average grain sizes were about 50 and 60 nm for Au and Ag samples. The thicknesses of the films are chosen to exceed the skin depth of Au and Ag, so that the measurements are expected to represent the optical properties of bulk metals.

To measure the optical properties at high temperature, the samples were placed on a resistive heating stage. It is known that surface oxidation will occur when Ag is heated to a high temperature. In order to avoid the surface oxidation, the heating stage holding the Ag sample was placed into a heating chamber, and argon as a shielding gas was continuously injected into the chamber during the measurement. Because Au is more stable than Ag, the ellipsometry measurements of Au films were performed under ambient conditions. The experiments were performed in the spectral range from 2 to 20 μm and temperature range from 300 to 700 K. The measurements of Au films were taken at incidence angles of 60°, 70°, and 80°, while the measurements of Ag films were taken at an incidence angle of 70° due to the limitation of optical windows on the heating chamber. Details about the theory of VASE and the method to extract dielectric function can be found in Ref. [41].

IV. RESULTS AND DISCUSSION

The electronic band structure is necessary for the calculation of electron-phonon and electron-electron scattering, so the accurate calculation of electronic eigenenergy is of crucial importance. The calculated electronic band structures and density of states of noble metals Au, Ag, and Cu at 0 K are depicted in Fig. 2, with the contribution of s, p, and d atomic orbitals indicated by different colors. The calculated electronic band structures are consistent with previous studies [42,43]. Figure 2(b) shows the band structure of Ag. It is shown that the parabolic band structure is intervened by the less dispersive curves of $4d$ electrons centered at about 3 eV below the Fermi energy, meaning that the $5s$ and $5p$ free-electron like states are hybridized with the $4d$ states to form a composite band. Additionally, the $4d$ electrons are distributed in a rather narrow energy range, which can be clearly seen from the density of states. The band structure of Au and Cu resembles that of Ag except that the d electrons in Ag are more localized than in Au. The d bands of Ag are lower in energy compared with Cu and Au, indicating that Ag is more free-electron like than Cu and Au.

In order to get the intraband dielectric function from theoretical calculations, the plasma frequency and electron scattering rate have to be determined from electronic structure calculations. The calculated Ω_p and τ_{ep}^{-1} at different temperatures are given in Table I. Here, Ω_p and τ_{ep}^{-1} can be extracted from experimental data by fitting the measured dielectric functions to the Drude model. The detailed fitting processes are given in the Supplemental Material [25]. The values of Ω_p and τ_{ep}^{-1} for Au and Ag obtained from our VASE measurements are also shown in Table I. The measured dielectric functions by VASE will be shown below. The plasma frequency for Au, Ag, and Cu from other experimental measurements are 8.45 eV [6], 8.9 eV [9], and 8.4 eV [44], respectively, which are in good agreement with our theoretical values. The calculated plasma frequency decreases with increasing temperature, which is in accordance with other theoretical prediction. The intraband plasma frequency can be expressed as $\Omega_p^2 = 4\pi ne^2/m_{\text{eff}}$. As temperature increases, the conduction-electron density n decreases with the increasing lattice constant, leading to the decreased plasma frequency. The plasma frequencies fitted from experimental results are also affected by extrinsic effects such as surface oxidation or impurity void fraction. Sundari *et al.* [8] found an increase in Ω_p and attributed it to a decrease in the void fraction of silver thin films. The electron-phonon scattering rates τ_{ep}^{-1} of noble

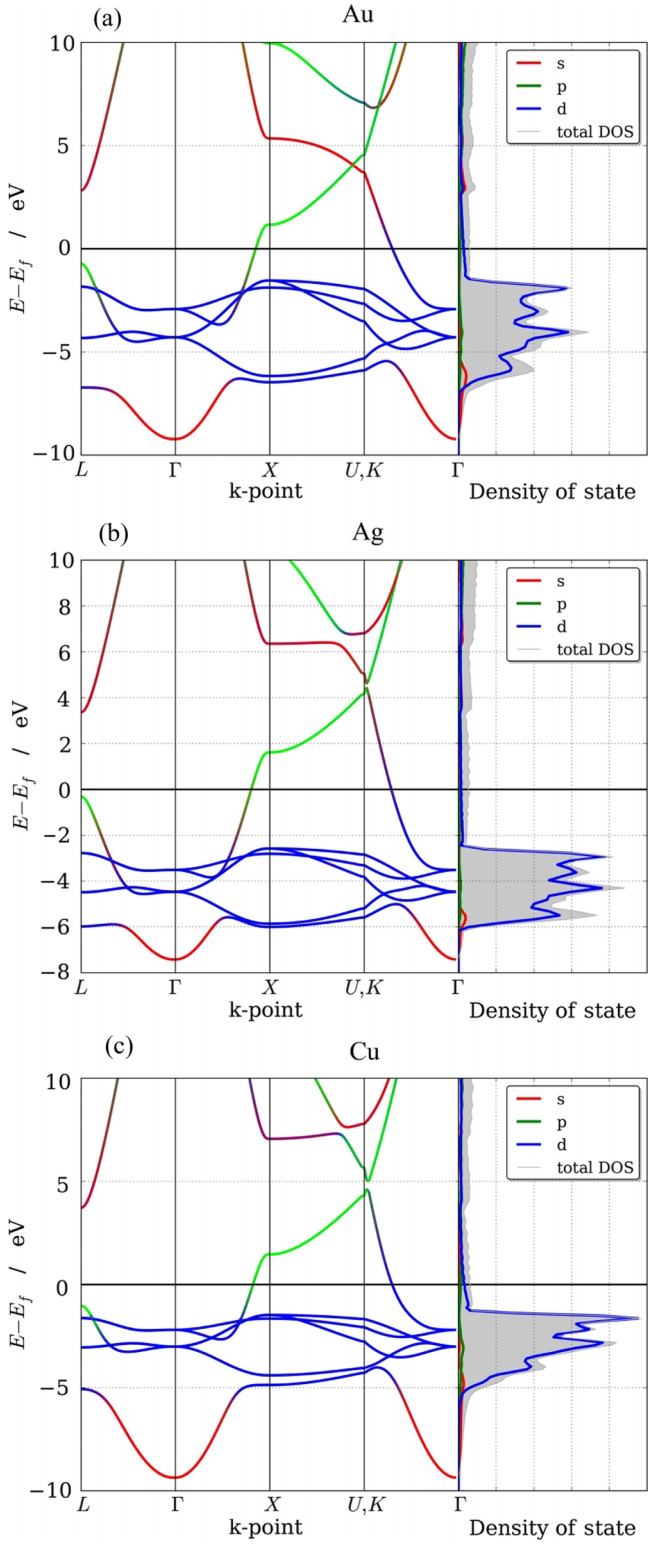

FIG. 2. Electronic band structures and density of states of Au, Ag, and Cu at 0 K.

metals are also given in Table I. The calculated τ_{ep}^{-1} shows an increasing trend as the temperature increases. It can be explained by the increased number of phonons and enhanced electron-phonon interaction as temperature increases. The comparison of the calculated τ_{ep}^{-1} with experimental results

TABLE I. The calculated plasma frequency $\Omega_p(T)$ and electron scattering rate $\tau_{ep}^{-1}(T)$. The experimental results of Au and Ag are obtained by fitting our measured dielectric functions by VASE to the Drude model. The experimental results of Cu were taken from Ref. [44].

		$\Omega_p(T)$ (eV)		$\tau_{ep}^{-1}(T)$ (meV)	
	T (K)	Calculated	Experimental	Calculated	Experimental
Au	100	8.7149		13.3274	
	300	8.6885	8.5884	33.9564	44.8007
	500	8.6497	8.9848	53.253	55.9401
	700	8.6131	9.0754	70.4556	74.5183
Ag	100	8.9357		6.4482	
	300	8.8998	9.3168	20.8698	40.0432
	500	8.8579	9.2555	42.9228	51.1293
	700	8.8131	9.1073	68.9936	64.7929
Cu	100	8.9477		9.4122	
	300	8.9191	8.4[a]	28.1164	34.5[a]
	500	8.8751		39.5442	
	700	8.8344		52.0554	

[a]The experimental data of Cu was taken from Ref. [44].

are presented in Table I. The calculated τ_{ep}^{-1} are smaller than that of experimental measurements, and the deviations mainly arise from the scattering by surface, grain boundary, and impurity/defect, which will be discussed below.

The electron-electron scattering plays an important role in the near infrared and visible spectral range, which cannot be neglected in the prediction of total scattering rate τ_D^{-1}. Based on the GW approximation, electron-electron scattering rates τ_{ee}^{-1} are calculated by Eq. (11), and the results are shown in Fig. 3. The calculated results can be fitted by a quadratic curve $\tau_{ee}^{-1}(\omega) = \beta(\hbar\omega)^2$, in accordance with the Fermi liquid theory [45]. The experimental results [19,46,47] by time-resolved two-photon photoemission (TR-2PPE) spectroscopy are shown in Fig. 3. Additionally, the theoretical calculations of τ_{ee}^{-1} by Lawrence's approximation [Eq. (10)] are shown in Fig. 3. The temperature-dependent part in Eq. (10) is neglected due to its small contribution. The overall agreement of calculated τ_{ee}^{-1} with experimental value demonstrates that GW approximation is able to reveal the electron-electron scattering process in noble metals. By including $\tau_{ee}^{-1}(\omega)$ in τ_D^{-1}, we get a frequency-dependent scattering rate $\tau_D^{-1}(\omega)$.

The relaxation time of surface scattering τ_s can be evaluated from Eq. (13). In this paper, we get $\tau_s = 43.49$ fs for Au, $\tau_s = 44.63$ fs for Ag, and $\tau_s = 37.51$ fs for Cu. Due to the anomalous skin effects in noble metals, τ_s should be included in the calculation of the total scattering rate τ_D^{-1}. The calculated temperature-dependent scattering rates are compared with the available experimental results in Fig. 4. In the infrared spectral range, the electron-electron scattering can be neglected, so they are not considered here. The calculated electron-phonon scattering rates are smaller than the scattering rates extracted from experimental measurements. After the inclusion of τ_s, the theoretical results of Au and Ag agree well with the experimental data [7,8], demonstrating the nontrivial contribution from surface scattering. The electron scattering

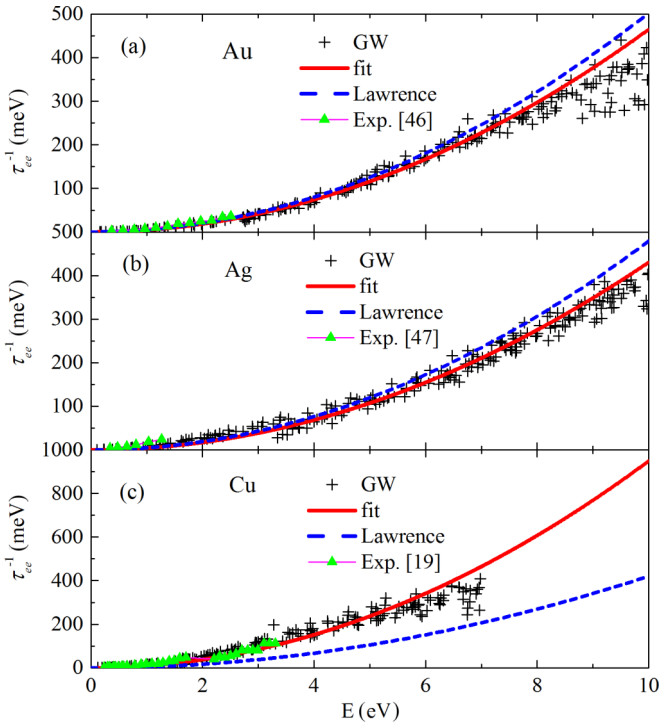

FIG. 3. Comparison of the electron-electron scattering rate of Au, Ag, and Cu from GW approximation with Lawrence's approximation and experimental measurements [19,46,47].

rates from our VASE experiments are also given in Fig. 4. As temperature increases, the difference between VASE results and $\tau_{ep}^{-1} + \tau_s^{-1}$ increases. The deviation may arise from the

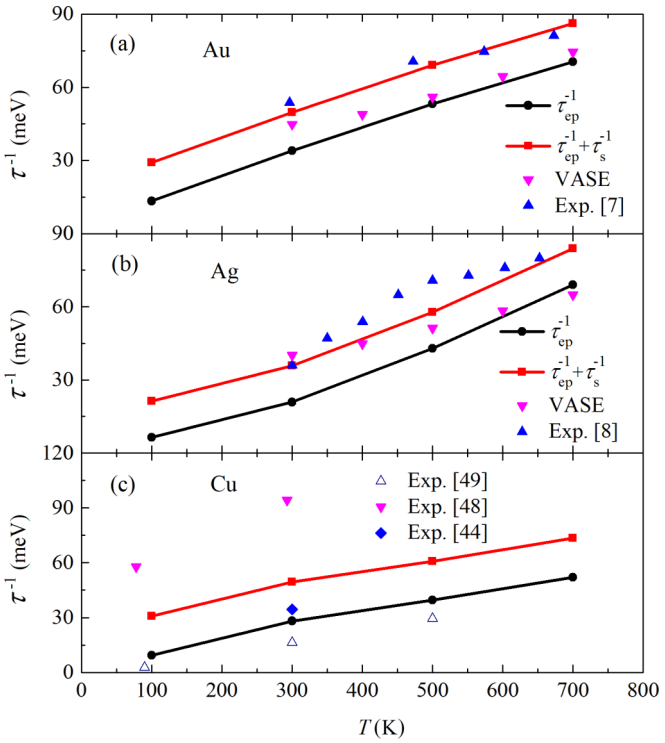

FIG. 4. The temperature dependence of the scattering rate of Au, Ag, and Cu from theoretical calculations and experimental measurements [7,8,44,48,49].

assumption of Eq. (13) that electrons scatter diffusely at the surface of noble metals, since the fraction of specularly scattered electrons is related to the surface roughness of the samples which will change with the increase of temperature [33]. Other experimental uncertainties, such as grain boundary scattering or impurity/defect scattering, also have influence on τ_D^{-1}. The calculated τ_D^{-1} of Cu shows large deviations from experimental results [44,48,49]. This is partly due to the errors during experimental measurements since surface oxidation is more likely to occur for Cu and the results of different experiments show large deviations. As is shown in Fig. 4, the increase of τ_{ep}^{-1} slows down for Au and Cu, in accordance with experimental measurements, but the increase of τ_{ep}^{-1} speeds up for Ag, which deviates from the experimental results. The Debye temperature Θ for Au, Ag, and Cu was 185, 220, and 310 K, respectively. Therefore, the upper limit of the integral in Eq. (7) $\Theta/T < 1$ applies for the high temperature range. By using Taylor's series $e^z \approx 1 + z$, Holstein's expression [Eq. (7)] can be approximated as

$$\frac{1}{\tau_{ep}} = \frac{1}{\tau_0}\left[\frac{2}{5} + \frac{T}{\Theta}\right], \tag{15}$$

which indicates the linear correlation of τ_{ep}^{-1} with T at high temperature. The deviation of τ_{ep}^{-1} calculated from first principles and Holstein's expression mainly arises from the differences in electronic band structures of noble metals.

With the calculated Ω_p and $\tau_D^{-1}(\omega)$, the intraband dielectric function of noble metals at room temperature can be obtained from Eq. (3). As is shown in Fig. 5, the intraband absorption dominates at lower energy. The intersection of intraband and interband dielectric function is different for Au, Ag, and Cu, which can be explained by the different locations of d bands in Au, Ag, and Cu. The interband dielectric functions of noble metals at room temperature are also shown in Fig. 5 with the experimental data from literature [6,9,49–52]. It can be observed that, while the theoretical calculation can reproduce the main features of experimental data, the calculated results present a red shift of the absorption edge compared with the experimental results, which is due to the approximation of exchange-correlation potential with the GGA [24]. The problem can be solved by the complicated time-dependent DFT or the GW method, which is widely used in the calculation of electronic properties of insulators and semiconductors. In this paper, the SO is applied to match the peak positions observed in the dielectric spectra. An SO of 0.9 eV is applied to Ag, while 0.5 and 0.4 eV are applied to Au and Cu, respectively.

The calculated intraband and interband dielectric functions are superimposed to get the total dielectric functions in the whole infrared-visible-ultraviolet spectral range. The predicted imaginary part of dielectric functions ε_2 in the temperature range of 100–700 K are shown in Fig. 6. In the near-infrared where $\omega \gg \tau_D^{-1}$, Eq. (3) can be simplified as $\varepsilon_2 \approx \Omega_p^2 \tau_D^{-1}/\omega^3$, ε_2 increases as the $\tau_D^{-1}(T)$ increases. Instead, in the far-infrared where $\omega \ll \tau_D^{-1}$, Eq. (3) can be simplified as $\varepsilon_2 \approx \Omega_p^2/\omega\tau_D^{-1}$, ε_2 decreases with the increase of $\tau_D^{-1}(T)$. The increasing trends of ε_2 with temperature are different for Au, Ag, and Cu, which can be explained by the tendency

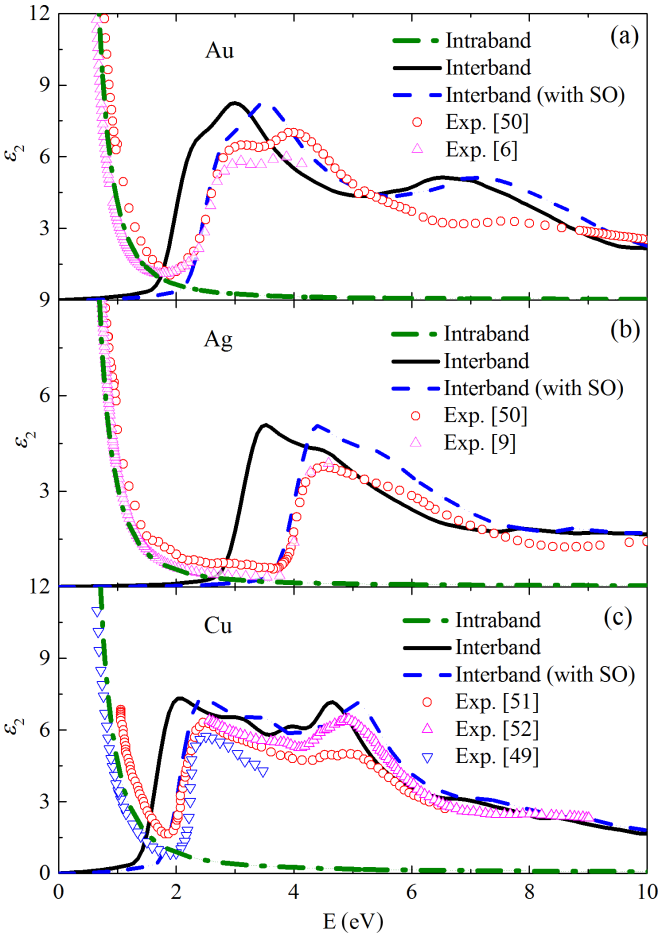

FIG. 5. Comparison of the calculated intraband and interband dielectric functions of Au, Ag, and Cu with experimental data [6,9,49–52] at room temperature. The interband dielectric functions adjusted by the SO are shown by dashed line.

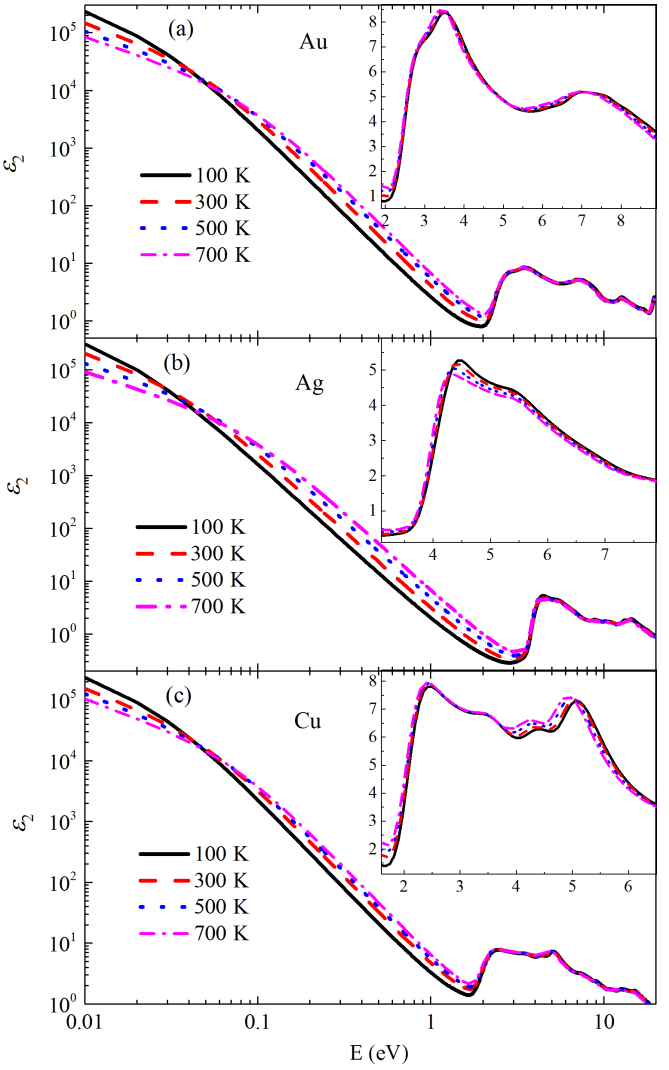

FIG. 6. Temperature-dependent imaginary part of theoretically calculated dielectric functions of Au, Ag, and Cu.

of $\tau_D^{-1}(T)$ arising from electron-phonon scattering. The inset in Fig. 6 shows the visible-ultraviolet dielectric functions of Au, Ag, and Cu, which were determined by the interband transitions of electrons. Theoretically, the interband dielectric functions of solids at finite temperature can be calculated by the temperature-dependent Bethe-Salpeter equation (TDBSE) [53]. So far, the TDBSE has been only applied to insulators and semiconductors, such as Si [53], GaN [54], and MoS_2 [55]. The calculation of finite temperature interband dielectric function of metal is still challenging. According to Winsemius *et al.* [37] the temperature dependence of the interband dielectric function of noble metals mainly arises from the changes of electronic band structure resulting from lattice expansion. In this paper, we calculate the interband dielectric function of noble metals by substituting the lattice constants of noble metals at finite temperatures. As is shown in Fig. 6, the location of the absorption peak shifts to the lower energy slightly as temperature increases, which is in accordance with experimental results [37]. The temperature effects in Ag and Cu are stronger than that of Au, which can be explained by the different thermal expansion coefficients of Au, Ag, and Cu. According to the experimental measurements [39,40], the thermal expansion coefficient of Ag at 300 K is $1.9 \times 10^{-5}\,\mathrm{K}^{-1}$, while that is $1.7 \times 10^{-5}\,\mathrm{K}^{-1}$ for Cu and $1.4 \times 10^{-5}\,\mathrm{K}^{-1}$ for Au.

The dielectric functions of Au and Ag by spectroscopic ellipsometry are shown in Fig. 7. The measurements are performed in the spectral range of 2–20 μm (0.06–0.61 eV), and temperature range of 300–700 K. The imaginary part of the dielectric functions increases monotonically with the increasing temperature. It can be seen from Fig. 7 that there are fluctuations in the measured ε_2, and the fluctuations of Ag are stronger than those of Au. Such effects may result from the surface morphology of Ag and optical window of heating chamber. Yang *et al.* [9] pointed out that deviations between experimental results and Drude model arise from intrinsic effects such as band structure, electron-electron scattering, and electron-phonon scattering, as well as extrinsic effects of surface, impurity, and grain boundary scattering. In our theoretical calculation, only the intrinsic effects and surface scattering have been included. As is known, the influence of surface oxidation, void fraction, etc. is unavoidable for Ag during the measurements. The temperature-dependent optical

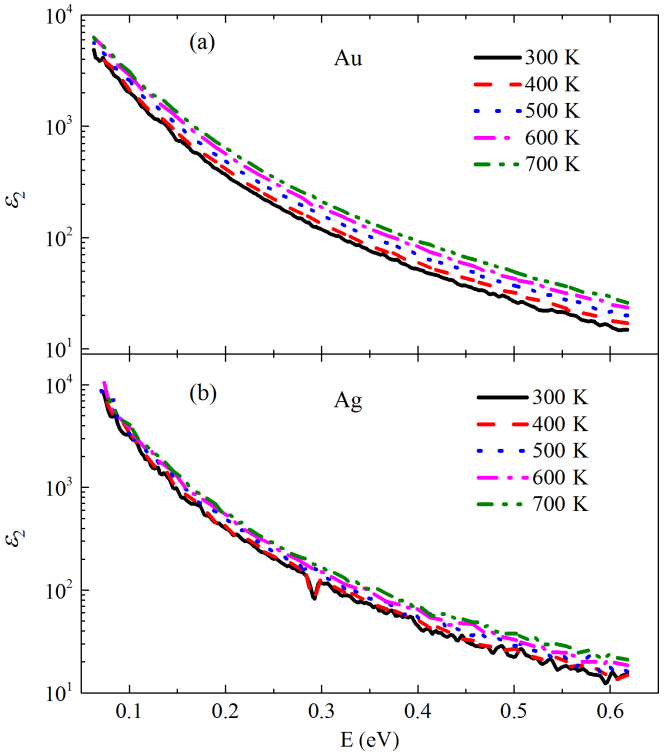

FIG. 7. Temperature-dependent imaginary part of dielectric functions of Au and Ag from VASE.

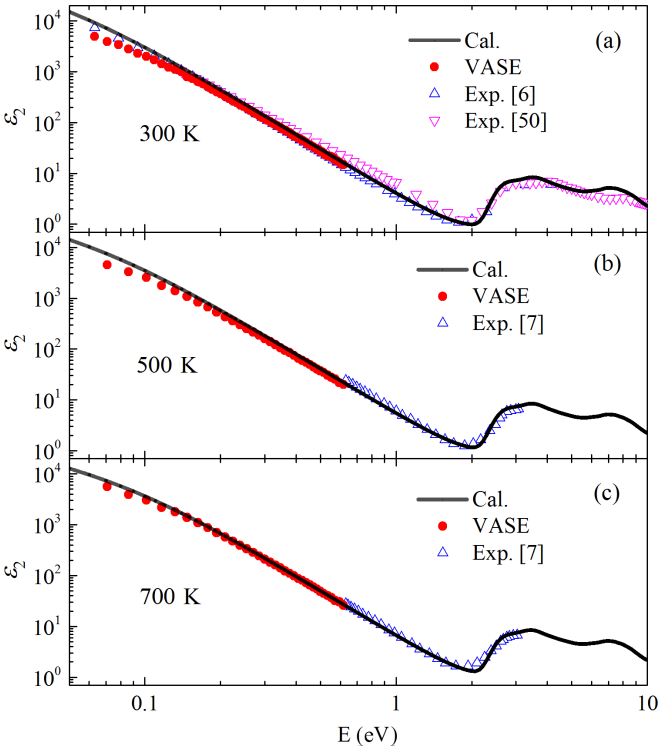

FIG. 8. The comparison of the theoretically calculated dielectric functions of Au with our VASE results and experimental results in Refs. [6,7,50] at different temperatures.

properties of Ag in the spectral range 1.4–3 eV have been measured by Sundari *et al.* [8] and Chen *et al.* [56], but their results contradict with each other. Sundari *et al.* [8] found an increase of ε_2 with the increase of temperature, but Chen *et al.* [56] showed a decrease of ε_2. Despite numerous studies, an explicit explanation of relationship between extrinsic effects and ε_2 have not been performed.

The comparison of the calculated dielectric functions of Au with the experimental results [6,7,50] are presented in Fig. 8. The imaginary part of the dielectric function by VASE in this paper at room temperature agrees well with the measurement of Ref. [6], which verifies the accuracy of our VASE experiment. The overall agreement between experiments and theoretical calculations is good, which validates the feasibility to predict the optical properties of Au at elevated temperature by electronic structure calculations. A deviation of the calculated dielectric function from experimental results can be noted below 0.1 eV, which is also observed by previous experimental measurement [9]. We applied quadratic frequency dependence of $1/\tau$ in this paper, while the authors of Ref. [9] found an exponential increase of τ in the low-frequency range, but the cause for such exponential increase is not clear. As is shown in Fig. 8, the deviation diminishes as temperature increases, indicating that the exponential increase of τ is mainly determined by the electron-electron scattering, and the electron-phonon scattering will dominate the temperature dependence at high temperature. Generally, the good agreement in the near infrared range indicates that the extrinsic effects, such as surface oxidation, impurity, and grain boundary scattering, in Au are negligible when compared with the intrinsic effects. Yang *et al.* [9] also demonstrated by experiments that the dielectric function of Au is less sensitive to variations in morphology than that of Ag.

The comparison of the calculated dielectric functions of Ag with the experimental results [8,9,50,56] are presented in Fig. 9. The overall agreements between the calculated ε_2 and experimental results are good, but the calculated results show small deviations from experimental results at elevated temperatures. Even the measurements from different studies deviate from each other, indicating the influence of extrinsic effects. In order to avoid surface oxidation, Sundari *et al.* [8] placed the sample in a high vacuum chamber maintained at a vacuum of $\sim 10^{-7}$ mbar, and the average grain size was 17.44 nm. In the experiment of Chen *et al.* [56], a SiO_x layer of 100 nm is coated onto the Ag film with a thickness of 100 nm. Yang *et al.* [9] verified that the dielectric function of Ag is more sensitive to variation in morphology than that of gold, and the grain size also has influence on the dielectric function. Additionally, impurity/defect scattering due to different preparation procedures for samples will increase the electron scattering rate. The grain size of the sample Yang *et al.* [9] used in their experiment was about 100 nm, and was larger than the mean-free path of the electron for silver which is about 30 nm at room temperature. The smaller grain size of sample used by Sundari *et al.* [8] leads to larger scattering rate, thus results in larger ε_2, as is show in Figs. 9(b) and 9(c). The deviation of Chen *et al.* [56] may arise from the influence of the SiO_x layer, since the grains

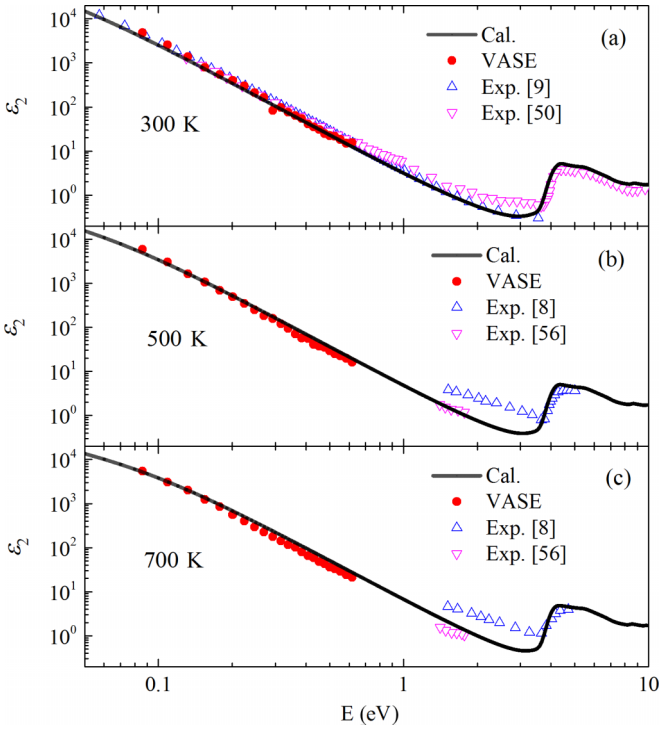

FIG. 9. The comparison of the theoretically calculated dielectric functions of Ag with VASE results and experimental results in Refs. [8,9,50,56] at different temperatures.

grow with increasing temperature while being geometrically constrained by the SiO_x layer, and the enlarged grains lead to smaller dielectric function. The grain size of the samples used in this paper is about 50 nm, which is larger than the mean-free path of the electron, and the influence of grain size on the optical properties is relatively small.

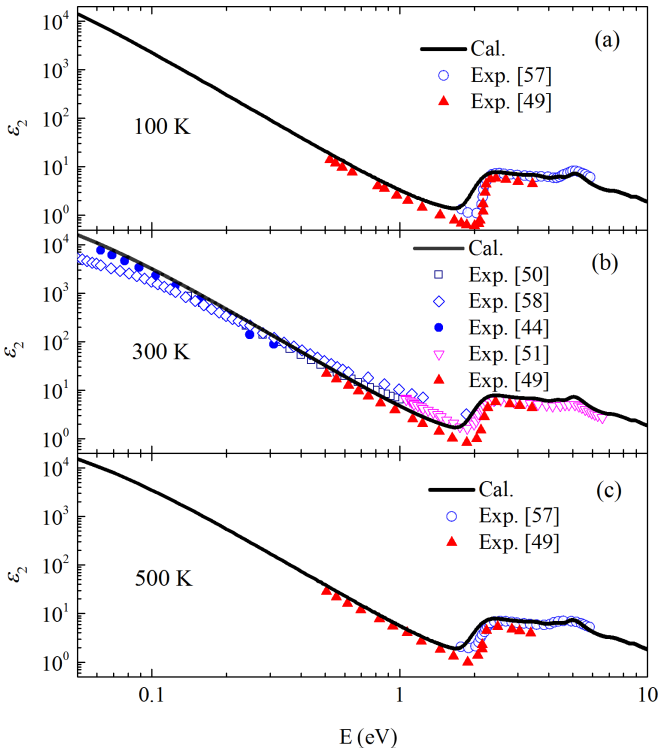

FIG. 10. The comparison of the theoretically calculated dielectric functions of Cu with experimental results in Refs. [44,49–51,57,58] at different temperatures.

In Fig. 10, the calculated dielectric functions of Cu at temperatures of 100, 300, and 500 K are compared with available experimental results from Refs. [44,49–51,57,58]. As is shown in Fig. 10, the calculated ε_2 demonstrates an overall good agreement with experimental measurements. The absorption edge in ε_2 is very steep at low temperature, which is related to excitonlike effects or the flatness of the d band. As temperature increases, the slope of the edge becomes gentle arising from the electron-phonon interaction. Most of the measurements in the literature are performed at room temperature, and there are few experimental results at elevated temperatures. The only experimental measurement for high temperature infrared dielectric function of Cu we can find in the literature was done in 1960 by Roberts [49]. Roberts found an increase of ε_2 with temperature, which is in accordance with our prediction, but the experiment of Roberts was performed only in the near infrared up to the temperature of 500 K. Due to the occurrence of high temperature oxidation, the experimental measurements of Cu were not done in this paper. The calculation in this paper will provide the dielectric functions of Cu in the energy range of 0.01–20 eV and temperature range of 100–700 K.

V. CONCLUSIONS

In summary, we have investigated the temperature dependence of dielectric functions of noble metals Au, Ag, and Cu using electronic structure calculations and spectroscopic ellipsometry experiments. Upon considering the electron-phonon, electron-electron, and electron-surface scattering, the calculated dielectric functions at finite temperature show good agreement with the experimental data. The total dielectric functions can be decomposed into the intraband and interband parts, and described by the Drude model and the interband transition theory, respectively. For the Drude model, the electron lifetime is determined by computing the intrinsic electron-electron, electron-phonon, and surface scattering. By comparing the individual contribution, it is found that the electron-phonon scattering mainly determines the temperature dependence of electron lifetime and thus intraband dielectric function. Within the scheme of interband transition theory, the influence of thermal expansion on interband dielectric function is determined, where the redshift of the absorption peak in the visible-ultraviolet spectral range is observed. In addition to theoretical calculations, the spectroscopic ellipsometry experiments were performed to measure the dielectric functions of Au and Ag over the temperature range of 300–700 K. The theoretical calculations show good agreement with our ellipsometry experiments and experiments from literature, which validates the theoretical method to predict the temperature-dependent dielectric functions of noble metals.

ACKNOWLEDGMENTS

This paper is supported by the National Natural Science Foundation of China (Grant Nos. 51336002 and 51421063).

[1] S. Linic, P. Christopher, and D. B. Ingram, Nat. Mater. **10**, 911 (2011).

[2] M. Bernardi, J. Mustafa, J. B. Neaton, and S. G. Louie, Nat. Commun. **6**, 7044 (2015).

[3] A. Naldoni, F. Riboni, U. Guler, A. Boltasseva, V. M. Shalaev, and A. V. Kildishev, Nanophotonics **5**, 112 (2016).

[4] T. L. Temple, Plasmonics **10**, 455 (2014).

[5] R. T. Beach and R. W. Christy, Phys. Rev. B **16**, 5277 (1977).

[6] R. L. Olmon, B. Slovick, T. W. Johnson, D. Shelton, S.-H. Oh, G. D. Boreman, and M. B. Raschke, Phys. Rev. B **86**, 235147 (2012).

[7] H. Reddy, U. Guler, A. V. Kildishev, A. Boltasseva, and V. M. Shalaev, Opt. Mater. Express **6**, 2776 (2016).

[8] S. T. Sundari, S. Chandra, and A. K. Tyagi, J. Appl. Phys. **114**, 033515 (2013).

[9] H. U. Yang, J. D'Archangel, M. L. Sundheimer, E. Tucker, G. D. Boreman, and M. B. Raschke, Phys. Rev. B **91**, 235137 (2015).

[10] T. Holstein, Ann. Phys. **29**, 410 (1964).

[11] W. E. Lawrence, Phys. Rev. B **13**, 5316 (1976).

[12] V. P. Zhukov, E. V. Chulkov, and P. M. Echenique, Phys. Rev. B **72**, 155109 (2005).

[13] M. Cazzaniga, Phys. Rev. B **86**, 035120 (2012).

[14] S. Poncé, E. R. Margine, C. Verdi, and F. Giustino, Comput. Phys. Commun. **209**, 18 (2016).

[15] A. Jain and A. J. H. McGaughey, Phys. Rev. B **93**, 081206 (2016).

[16] Y. Wang, Z. Lu, and X. Ruan, J. Appl. Phys. **119**, 225109 (2016).

[17] J. I. Mustafa, M. Bernardi, J. B. Neaton, and S. G. Louie, Phys. Rev. B **94**, 155105 (2016).

[18] U. Mizutani, *Introduction to the Electron Theory of Metals* (Cambridge University Press, New York, 2001).

[19] M. Bauer, A. Marienfeld, and M. Aeschlimann, Prog. Surf. Sci. **90**, 319 (2015).

[20] D. Y. Smith and B. Segall, Phys. Rev. B **34**, 5191 (1986).

[21] G. Grosso and G. P. Parravicini, *Solid State Physics, 2nd Ed.* (Academic Press, Amsterdam, 2013).

[22] J. Harl, Ph.D. thesis, University of Vienna, 2008.

[23] J. Hafner, J. Comput. Chem. **29**, 2044 (2008).

[24] R. M. Martin, *Electronic Structure: Basic Theory and Practical Methods* (Cambridge University Press, New York, 2004).

[25] See Supplemental Material at http://link.aps.org/supplemental/10.1103/PhysRevB.96.115154 for details on the AFM results of Au and Ag sample surface, convergence test, fit quality of Drude model, and empirical functions of the temperature-dependent intraband dielectric function.

[26] J. A. McKay and J. A. Rayne, Phys. Rev. B **13**, 673 (1976).

[27] G. R. Parkins, W. E. Lawrence, and R. W. Christy, Phys. Rev. B **23**, 6408 (1981).

[28] P. Giannozzi, S. Baroni, N. Bonini, M. Calandra, R. Car, C. Cavazzoni, D. Ceresoli, G. L. Chiarotti, M. Cococcioni, I. Dabo, A. Dal Corso, S. de Gironcoli, S. Fabris, G. Fratesi, R. Gebauer, U. Gerstmann, C. Gougoussis, A. Kokalj, M. Lazzeri, L. Martin-Samos *et al.*, J. Phys.-Condes. Matter **21**, 395502 (2009).

[29] C. Hartwigsen, S. Goedecker, and J. Hutter, Phys. Rev. B **58**, 3641 (1998).

[30] F. Giustino, M. L. Cohen, and S. G. Louie, Phys. Rev. B **76**, 165108 (2007).

[31] R. B. Dingle, Physica **19**, 729 (1953).

[32] T. Holstein, Phys. Rev. **88**, 1427 (1952).

[33] H. E. Bennett, J. M. Bennett, E. J. Ashley, and R. J. Motyka, Phys. Rev. **165**, 755 (1968).

[34] N. Ashcroft and K. Sturm, Phys. Rev. B **3**, 1898 (1971).

[35] B. Gamez and J. Ocana, J. Phys. D-Appl. Phys. **33**, 305 (2000).

[36] B. Huttner, J. Phys.-Condes. Matter **8**, 11041 (1996).

[37] P. Winsemius, F. F. Van Kampen, H. P. Lengkeek, and C. G. Van Went, J. Phys. F: Met. Phys. **6**, 1583 (1976).

[38] N. E. Christensen and B. Seraphin, Phys. Rev. B **4**, 3321 (1971).

[39] F. C. Nix and D. Macnair, Phys. Rev. **60**, 597 (1941).

[40] F. C. Nix and D. Macnair, Phys. Rev. **61**, 74 (1942).

[41] J. Y. Yang, W. J. Zhang, L. H. Liu, J. Qiu, K. Wang, and J. Y. Tan, J. Chem. Phys. **141**, 104703 (2014).

[42] A. Marini, G. Onida, and R. Del Sole, Phys. Rev. Lett. **88**, 016403 (2001).

[43] T. Rangel, D. Kecik, P. E. Trevisanutto, G.-M. Rignanese, H. Van Swygenhoven, and V. Olevano, Phys. Rev. B **86**, 125125 (2012).

[44] M. A. Ordal, L. L. Long, R. J. Bell, S. E. Bell, R. R. Bell, R. W. Alexander, and C. A. Ward, Appl. Opt. **22**, 1099 (1983).

[45] W.-D. Schöne, Prog. Surf. Sci. **82**, 161 (2007).

[46] J. Cao, Y. Gao, H. E. Elsayed-Ali, R. J. D. Miller, and D. A. Mantell, Phys. Rev. B **58**, 10948 (1998).

[47] M. Wolf and M. Aeschlimann, Physikalische Blätter **54**, 154 (1998).

[48] P. B. Johnson and R. W. Christy, Phys. Rev. B **11**, 1315 (1975).

[49] S. Roberts, Phys. Rev. **118**, 1509 (1960).

[50] E. D. Palik, *Handbook of Optical Constants of Solids* (Academic Press, New York, 1998).

[51] P. B. Johnson and R. W. Christy, Phys. Rev. B **6**, 4370 (1972).

[52] K. Stahrenberg, T. Herrmann, K. Wilmers, N. Esser, W. Richter, and M. J. G. Lee, Phys. Rev. B **64**, 115111 (2001).

[53] A. Marini, Phys. Rev. Lett. **101**, 106405 (2008).

[54] H. Kawai, K. Yamashita, E. Cannuccia, and A. Marini, Phys. Rev. B **89**, 085202 (2014).

[55] A. Molina-Sánchez, M. Palummo, A. Marini, and L. Wirtz, Phys. Rev. B **93**, 155435 (2016).

[56] Y.-J. Chen, M.-C. Lee, and C.-M. Wang, Jpn. J. Appl. Phys. **53**, 08MG02 (2014).

[57] G. P. Pells and M. Shiga, J. Phys. C: Solid State Phys. **2**, 1835 (1969).

[58] M. A. Ordal, R. J. Bell, R. W. Alexander, L. L. Long, and M. R. Querry, Appl. Opt. **24**, 4493 (1985).